Carbohydrate Polymers 101 (2014) 565–573

Contents lists available at ScienceDirect

Carbohydrate Polymers

journal homepage: www.elsevier.com/locate/carbpol

Montmorillonite–levan nanocomposites with improved thermal and mechanical properties

Xiaoming Chen, Hongsheng Gao, Harry J. Ploehn*

Department of Chemical Engineering, University of South Carolina, Columbia, SC 29208, United States

ARTICLE INFO

Article history:
Received 13 July 2013
Received in revised form
18 September 2013
Accepted 21 September 2013
Available online 1 October 2013

Keywords:
Levan
Polysaccharide
Montmorillonite
Nanocomposite
Isotropic–nematic

ABSTRACT

This work reports on the structure and properties of novel nanocomposites composed of exfoliated montmorillonite clay blended with levan, a polysaccharide produced by *Bacillus* sp. Dry levan is very brittle, making it difficult to obtain stand-alone films. MMT–levan composites were prepared by solution blending in water, coating on plastic surfaces, partial drying at 50 °C, and conditioning in air at 50–60% relative humidity. This process results in freestanding, transparent, and flexible films of pure levan and MMT–levan composites plasticized by 10–15 wt% water. XRD patterns from levan–MMT composites indicate an MMT interlayer spacing 0.62 nm greater than that of the starting MMT, suggesting re-stacking of MMT platelets coated by adsorbed, uncoiled levan molecules. FTIR results suggest that levan adheres to MMT via water-mediated hydrogen bonding between the levan's hydroxyl groups and MMT surface oxygens. MMT–levan composites have improved thermal stability and a well-defined glass transition temperature that increases with MMT loading. The tensile moduli of levan–MMT composites increase by as much as 480% relative to pure levan. The XRD and mechanical property results suggest that MMT reinforces levan through a filler network structure composed of MMT platelets bridged by adsorbed levan molecules, enhanced when the MMT loading becomes high enough (5–10 wt% MMT) to induce an isotropic–nematic transition in MMT platelet orientation.

1. Introduction

Polysaccharides offer considerable promise as sustainable, biodegradable materials for packaging and other applications (Johansson et al., 2012; Majeed et al., 2013; Tang, Kumar, Alavi, & Sandeep, 2012). Polysaccharides extracted from plants, such as cellulose, hemicellulose, starch, pectin, and chitin, have received much attention (Chivrac, Pollet, & Averous, 2009; Rhim & Ng, 2007; Sinha Ray & Bousmina, 2005; Sorrentino, Gorrasi, & Vittoria, 2007; Yu, Dean, & Li, 2006), perhaps because their source materials are widely available in mass quantities and at low cost. Exopolysaccharides secreted by microbes often have well-defined structure and high molecular weight (French, 1989), but they have received less attention because they have not been readily available in large quantities and high purity. Advances in microbial fermentation have resulted in increasing availability of high purity, well characterized biopolymers, especially polyhydroxyalkanoates (Johansson et al., 2012; Sinha Ray & Bousmina, 2005; Sorrentino et al., 2007; Tang et al., 2012; Yu et al., 2006). Among the exopolysaccharides, levan has been produced by large-scale fermentation (Bodie, Schwartz, & Catena, 1985; Han & Watson, 1992; Keith et al., 1991; Kim et al., 2005; Küçülaşik et al., 2011; Liu et al., 2010; Poli et al., 2009; van Dyk, Kee, Frost, & Pletschke, 2012).

Levan and inulin are fructans, fructose-based polysaccharides produced by many plants and microorganisms (French, 1989). Levan consists of D-fructofuranosyl monomers joined by $\beta(2\rightarrow 6)$ linkages and branched via $\beta(2\rightarrow 1)$ linkages (Supporting information, Fig. S1). Plant fructans have relatively low degrees of polymerization (<100 fructofuranose monomers, or residues) with molecular weights on the order of 10^4 Da. Microbial levans, on the other hand, typically have higher degrees of polymerization (~10,000 residues) and molecular weights ($\sim 10^5$–10^7 Da). Chemical analyses in conjunction with ^{13}C NMR indicate that branching occurs on up to 30% of the residues in levan (Seymour, Knapp, & Jeanes, 1979; Simms, Boyko, & Edwards, 1990). Electron microscopy images (Ingelman & Siegbahn, 1944; Newbrun, Lacy, & Christie, 1971), data from light scattering and sedimentation (Bahary, Stivala, Newbrun, & Ehrlich, 1975; Stivala, Bahary, Long, Ehrlich, & Newbrun, 1975), small-angle X-ray scattering (Khorramian & Stivala, 1982; Stivala & Khorramian, 1982), and viscometry (Arvidson, Rinehart, & Gadala-Maria, 2006; Kasapis, Morris, Gross, & Rudolph, 1994) all agree that levan molecules in aqueous solutions do not undergo gelation with increasing solution

* Corresponding author. Tel.: +1 803 777 7307; fax: +1 803 777 8100.
E-mail address: ploehn@cec.sc.edu (H.J. Ploehn).

0144-8617/$ – see front matter © 2013 Elsevier Ltd. All rights reserved.
http://dx.doi.org/10.1016/j.carbpol.2013.09.073

concentration and have a compact, globular structure (spheroidal or ellipsoidal).

Levan's high molecular weight and water solubility make it attractive for various industrial applications, including cosmetics, pharmaceutical coatings, and adhesives (Combie, 2006; Kim et al., 2005; Kang et al., 2009) There have been only a few studies aimed at developing levan as a bio-based plastic for packaging applications. Barone and Medynets (2007) used compression molding and melt extrusion to prepare cohesive, pliable levan films plasticized by glycerol. Levan films containing less than 10 wt% glycerol were too brittle to be characterized by tensile testing. Films containing 10–35% glycerol had tensile moduli less than 0.1 GPa and glass transition temperatures (T_g) ranging from 60 °C (10 wt%) down to 0 °C (30 wt%). These property values are too low to permit the use of levan/glycerol films in packaging or structural applications. Manadhar, Vidhate, and D'Souza (2009) prepared levan fibers by electrospinning from concentrated solutions (60 wt%), but fiber mechanical properties were not reported. The poor mechanical properties of pure levan films are probably related to its molecular structure: despite its high molecular weight, levan's highly branched, compact globular structure does not permit significant intermolecular entanglement. This leads to brittleness in neat levan, and low tensile modulus in glycerol-plasticized levan.

Recent reviews (Chivrac et al., 2009; Johansson et al., 2012; Majeed et al., 2013; Rhim & Ng, 2007; Sinha Ray & Bousmina, 2005; Sorrentino et al., 2007; Tang et al., 2012; Yu et al., 2006) demonstrate that, in many cases, biopolymer nanocomposites have properties superior to those of the corresponding pure biopolymer. Examples of recent work in this vein are studies of xylan (Unlu, Gunister, & Atici, 2009; Viota, Lopez-Viota, Saake, Stana-Kleinschek, & Delgado, 2010) or xyloglucan (Kochumalayil et al., 2013) reinforced with MMT. The present work explores the possibility of improved thermal and mechanical properties for nanocomposites of exfoliated montmorillonite (MMT) dispersed in levan. Improved properties may extend levan's range of applications to include barrier packaging with unique features, such as edible packaging or accelerated biodegradability.

2. Experimental procedures

2.1. Materials

Levan powder derived from *Bacillus* sp. was obtained from Montana Polysaccharides (Winnsboro, SC). The as-received levan was dissolved in deionized water (~18 MΩ resistivity, Barnstead Nanopure) with prolonged stirring to produce a 10.0 wt% solution. The solution was centrifuged at 2000 rpm for 100 min at 20 °C (Eppendorf model 5403, Brinkmann) and the clear supernatant solution was retained. Samples of this solution were diluted and used for light scattering characterization. A concentrated stock solution of purified levan was prepared from the supernatant by removing water using a rotary evaporator. Dry weight analysis indicated that the solid content of the final levan stock solution was 27.5 wt%. In order to inhibit bacterial growth, 0.5 wt% sodium azide was added to the concentrated levan stock solution.

Sodium montmorillonite (MMT) clay (Cloisite® Na^+, Southern Clay Products) was dispersed in water using a procedure (Ploehn & Liu, 2006) known to produce suspensions containing >95% exfoliated MMT platelets. As-received MMT powder was added to deionized water to produce a 1.0 wt% suspension. The suspension was stirred continuously at room temperature for at least 24 h, ultrasonicated (model FS28, Fisher Scientific) for 30 min, and then centrifuged at 4000 rpm for 60 min to remove mineral contaminants and unexfoliated MMT. The supernatant MMT suspension was retained; dry weight analysis indicated a MMT concentration of 0.7 wt%. AFM characterization of suspensions prepared in this way (Ploehn & Liu, 2006) indicated nearly complete exfoliation of MMT into individual platelets with an average thickness of 0.97 nm. The MMT platelets have a log-normal distribution of aspect ratio with a mean of 166 ± 86 and a median of 147 (Ploehn & Liu, 2006).

2.2. Film preparation

MMT–levan nanocomposite films were prepared by solution blending of the stock levan solution (27.5 wt%) and the stock MMT suspension (0.7 wt%). Appropriate quantities of the levan solution and MMT suspension were blended so that the final solid films contained 0, 1.0, 5.0, or 10.0 wt% MMT. The aqueous levan–MMT blends were stirred for 60 min, ultrasonicated for 30 min, and then concentrated using a rotary evaporator, producing viscous coating suspensions containing approximately 5 wt% total solids (levan + MMT). The coating suspensions were coated onto Mylar® sheets using the drawdown coating method to prepare levan–MMT nanocomposite films. The wet films were dried in an air-circulated oven at 50 °C for approximately 2–4 h, determined through trial-and-error as optimal for removing most, but not all of the moisture. Insufficient drying produces tacky films that are difficult to peel, while complete drying produces brittle films that tend to crack when peeled from the Mylar®. After peeling, the films were conditioned in ambient air, at room temperature (~23 °C) and 50–60% relative humidity, to equilibrate the water content. The final film thickness varied from 80 to 280 μm, depending on the MMT content, coating suspension viscosity, and drawdown coating procedure.

2.3. Characterization methods

2.3.1. Solution characterization

We used UV–vis spectrophotometry (UV–vis) and static and dynamic light scattering (SLS, DLS) and to characterize levan's molecular structure and solution properties. Solution optical absorbance was characterized by UV-vis measurements (Shimadzu model UV-2101PC). Light scattering experiments employed a Brookhaven BI-200 goniometer, BI-9000AT correlator (Brookhaven Instruments) and Ar-ion laser (Lexel model 95; λ = 514.5 nm). For DLS, samples of stock levan solution were diluted with DI water and pH adjusted by titrating with 1.0 M NaOH or 37% HCl. Intensity autocorrelation data were analyzed using quadratic cumulants or CONTIN methods via the Brookhaven system software.

Prior to SLS, we measured the refractive index (n) of levan solutions of varying concentrations (Abbé Mark II refractometer) to determine the specific refractive index increment (dn/dc). For concentrations up to 50 mg/mL (~0.5 wt%), n varies linearly with c, yielding $dn/dc = 0.1427 \pm 0.0010$ mL/g, in excellent agreement with the value of Stivala et al. (1975). For SLS measurements, DI water was filtered three times using 0.2 μm cellulose acetate filters. The levan stock solution was either used unfiltered or filtered once with a 0.45 μm cellulose acetate filter, with subsequent dilution using filtered DI water. Scattered intensity, measured as a function of scattering angle θ and c, were analyzed via Zimm and Berry plots (Brookhaven software). We calibrated these measurements with solutions of a polystyrene standard (2.0×10^6 Da) in toluene (Fig. S2). The Berry plot yielded better agreement of the MW value. Thus Berry plots were used to determine radius of gyration (R_g), molecular weight (MW), and second virial coefficient (A_2) values.

2.3.2. Solid film characterization

Solid film samples were ground using a Wiley mill, and the powder was sieved with a #60 mesh screen. Wide-angle X-ray diffraction (WAXD) employed a powder diffractometer (Rigaku MiniFlex II) using Cu Kα radiation (λ = 1.5419 Å). Scattered intensity data were recorded from 3° to 40° (2θ) at a rate of 0.5° per min

and a step resolution of 0.02°. Thermogravimetric analysis (TGA, TA Instruments model SDT600) measured sample weight loss for heating in air from 35 °C to 650 °C ramped at 20 °C per min. Differential scanning calorimetry (DSC, TA Instruments DSC-Q200) characterized 10 mg samples in Tzero crimped pans. The first heating/cooling scan ramped the temperature (at a rate of 10 °C/min under N_2 purge per ASTM D3418) up to 200 °C and then down to 0 °C. The second heating scan ramped the temperature from 0 °C to 240 °C. The samples for both TGA and DSC were dried in vacuum at 80 °C for 24 h prior to testing. Comparing TGA results for non-dried and dried samples shows (vide infra) that this drying method effectively removes water from the samples.

FTIR spectra (Perkin-Elmer Spectrum 100) were collected from film specimens in the transmission mode at a resolution of 1 cm^{-1} and converted to absorbance by the Spectrum® software. UV–vis absorbance spectra were also collected from film specimens (Shimadzu model UV-2101PC with film holder).

Mechanical properties of solid films were characterized using dynamic mechanical analysis (DMA, TA Instruments model RSA-III). The tensile tests included strain-controlled, small-amplitude oscillatory tests as well as large deformation stress–strain measurements. All tests were carried out in air under ambient conditions (23 ± 1 °C, 55 ± 2% RH). In the oscillatory tests, constant-temperature frequency sweeps were used (rather than temperature sweeps) to avoid changes in water content. The frequency varied from 0.01 to 100 Hz with an applied strain of 0.05%. The test specimens were 40–50 mm long strips of uniform width (4–5 mm) and thicknesses (0.08–0.28 mm) that varied with MMT loading and coating conditions. All tests used a crosshead separation of 15 mm. The stress–strain tests employed a strain rate of 0.01% per second. For both kinds of tensile tests, at least five specimens were tested.

3. Results and discussion

3.1. Levan molecular properties

Previous studies (Huber & Viney, 1997, 1998; Huber, Stayton, Viney, & Kaplan, 1994) reported liquid crystal formation in levan solutions containing low concentrations of nucleic acid impurities. Gel electrophoresis of 5 wt% levan solution (Fig. S3) indicates no detectable nucleic acid impurities in the as-received *Baccilus* sp. levan from Montana Polysaccharides. The turbidity of levan solutions, measured at λ = 514.5 nm (Fig. S4), is independent of temperature (20–70 °C), increases nearly linearly with concentration (wt%), and shows no distinct transitions indicative of liquid crystal formation.

Levan molecules in the unfiltered solution have a mean diameter of 168 nm (55% CV), while the mean diameter of levan in the filtered solution (0.45 μm cellulose acetate filter) is 145 nm (54% CV) (Fig. S5). The size distributions look similar; both distributions are polydisperse with coefficients of variance (CV) of about 54%. However, we see subtle differences at the high end of the distributions. The weighted average of the last three bars in each distribution gives 318 nm for filtered levan, and 359 nm for unfiltered levan. This suggests that the cellulose acetate filter retains some of the largest, highest molecular weight levan molecules, as well as any large aggregates.

DLS size measurements with quadratic cumulants (QC) regression of the intensity autocorrelation function are repeatable and consistent with the DLS/CONTIN results. The mean diameters for levan molecules in unfiltered and filtered solutions are 158 ± 2 nm and 139 ± 2 nm, respectively (the ± values are 95% confidence intervals, $N = 8$ independent measurements). These DLS/QC values are slightly smaller than the DLS/CONTIN values but are in reasonable agreement. For solutions with varying pH, the mean diameter of levan molecules (DLS/QC) shows small but statistically significant variations (Fig. S6).

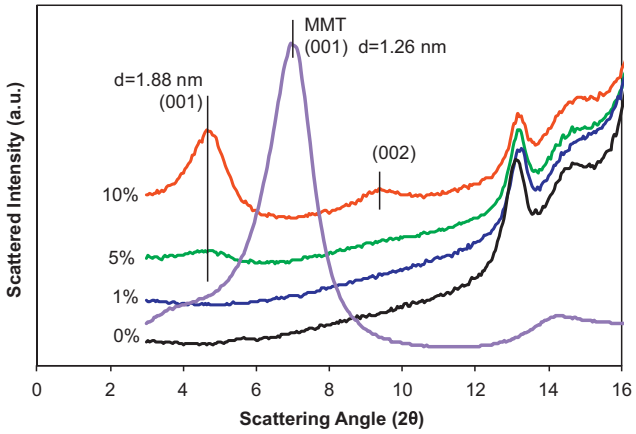

Fig. 1. Wide-angle X-ray diffraction patterns for pure levan (labeled 0%), MMT–levan composites (curves labeled with wt% MMT and shifted upwards for clarity), and pure MMT. Patterns for the angular range 0°-40° in 2θ are shown in Fig. S7.

Static light scattering provides additional information on molecular weight and intermolecular interactions. Fig. S7 shows typical Berry plots for unfiltered and filtered levan solutions. For unfiltered levan solutions, SLS gives $R_g = 91 \pm 4$ nm, MW = $(9.8 \pm 0.9) \times 10^6$ Da, and $A_2 = (1.3 \pm 1.7) \times 10^{-6}$ cm^3 mol/g^2 ($N = 5$, ± values are 95% confidence intervals). Twice the R_g value (182 nm) compares well with the hydrodynamic diameter values from DLS. The A_2 value does not differ significantly from zero, indicating that the levan molecules interact somewhat like hard spheres. The corresponding values for filtered levan solutions are $R_g = 76 \pm 1$ nm, MW = $(5.3 \pm 0.1) \times 10^6$ Da, and $A_2 = (13.9 \pm 1.1) \times 10^{-6}$ cm^3 mol/g^2 ($N = 8$). Again, twice the R_g value (152 nm) compares well with the diameter values from DLS. Filtration apparently removes the highest molecular weight molecules from solution. The small, positive A_2 value indicates that the remaining levan molecules have a weak repulsive interaction. These values may have some error since the filtration probably reduces the levan solution concentrations.

3.2. MMT–levan composite nanostructure

3.2.1. X-ray diffraction

The XRD pattern of purified, restacked "bare" MMT (Fig. S8) shows peaks at 7.1° 2θ (0 0 1), 14.2° 2θ (0 0 2), and 28.3° 2θ (0 0 4), from which we estimate an average *d*-spacing 1.26 nm. Pure levan has a distinctive peak pattern between 10° and 40° (Fig. S7), but no peaks in the 3–10° range (Fig. 1). The XRD patterns for MMT–levan composites (Fig. 1) do not have any peaks near 7.1° 2θ that would arise from unexfoliated MMT. The patterns for 5 and 10 wt% MMT–levan composites clearly show a peak at 4.7° 2θ, representing the (0 0 1) peak for MMT platelets with a *d*-spacing of 1.88 nm. The pattern for 10 wt% MMT–levan also shows the corresponding (0 0 2) peak (centered at 9.4° 2θ) for this *d*-spacing. The change in *d*-spacing (relative to restacked "bare" MMT), about 0.62 nm, suggests that in the composites, the restacked MMT platelets are separated by a layer of adsorbed, uncoiled levan molecules.

The starting stock suspension contained only exfoliated MMT platelets. In the composite XRD patterns, (0 0 1) and (0 0 2) peaks appear with increasing MMT loading, indicating increased order due to platelet re-stacking or alignment. Two different mechanisms combine to explain this observation. First, upon mixing stock MMT and levan solutions, levan adsorption onto MMT platelets may have resulted in bridging flocculation, leading to platelet re-stacking.

These stacks could be present in all of the composites, but the (0 0 1) diffraction peak becomes apparent when the scattering from MMT exceeds that from the levan and the baseline noise. However, bridging flocculation should result in aggregates with randomly oriented platelets.

A second mechanism, the isotropic–nematic (*I–N*) phase transition (Onsager, 1949), may promote alignment of MMT platelets in these composites. Reviews of *I–N* phase transition theory (Harnau, 2008; Vroege & Lekkerkerker, 1992), simulations (Bates, 1999; Bates & Frenkel, 1999), and experiments (van der Beek et al., 2006; van der Kooij, Kassapidou, & Lekkerkerker, 2000; van der Kooij & Lekkerkerker, 1998) report that nematic (stacking) ordering of disk-shaped particles begins at critical dimensionless concentration $\rho_I^* \equiv \rho_I \langle D^3 \rangle$ in the range of 3.5–4.0. Here platelet number density is defined as

$$\rho_I \equiv \frac{4\phi_I}{\pi \langle D^2 \rangle \langle L \rangle} = \frac{\rho_I^*}{\langle D^3 \rangle} \quad (1)$$

where ϕ_I is the platelet volume fraction, D and L are platelet equivalent disk diameter and thickness, and $\langle\rangle$ indicates an average value. Values of $\langle L \rangle$, $\langle D^2 \rangle$, and $\langle D^3 \rangle$ for our MMT suspension are available from AFM measurements (Ploehn & Liu, 2006); see Supporting Information, including L and D distributions for MMT platelets, Fig. S9). Assuming $\rho_I^* = 3.8$ as a plausible value (van der Beek et al., 2006), Eq. (1) gives $\phi_I = 0.016$ (1.6 vol%) for the onset of nematic ordering, equivalent to an MMT loading of 3.1 wt%, based on $\rho_{MMT} = 2.86\,g/cm^3$ and $\rho_{levan} = 1.4\,g/cm$ (Barone & Medynets, 2007; Majeed et al., 2013; Manadhar et al., 2009). Thus the (0 0 1) and (0 0 2) XRD peaks become increasingly prominent in the patterns for 5 and 10 wt% MMT–levan composites due to the onset of nematic ordering of the high aspect ratio MMT platelets. Mechanical property results (vide infra) provide additional evidence supporting this claim.

3.2.2. FT-IR spectroscopy

The FTIR absorbance spectrum of pure levan (Fig. 2a) agrees well with those previously published (Barone & Medynets, 2007; French, 1989; Grube, Bekers, Upite, & Kaminska, 2002; Küçülaşik et al., 2011; Liu et al., 2010; Poli et al., 2009; van Dyk et al., 2012). Detailed peak assignments may be found in these references. Several characteristic bands are of interest here, including the broad band centered at 3300 cm^{-1} (O—H stretching), a double peak at 2936 cm^{-1} and 2886 cm^{-1} (asymmetric and symmetric H—C—H stretching), a series of distinctive peaks in the 1500–1200 cm^{-1} range (C—H deformations), and several very strong peaks below 1200 cm^{-1} (C—O—C and C—O—H stretching, pyranose ring deformations). The peak at 1639 cm^{-1} has some conflicting assignments, including C=O (Poli et al., 2009), amides (Grube et al., 2002; van Dyk et al., 2012), and bound water (Barone & Medynets, 2007; Liu et al., 2010). Based on previous FTIR characterization of bound water in polysaccharides (Velazquez, Herrera-Gomez, & Martin-Polo, 2003), the high water content in our samples (vide infra), and the absence of detectable DNA impurities, we concur with previous studies associating this peak with the HOH scissoring deformation from bound water.

The FTIR spectrum for MMT (Fig. 2a) has typical strong bands at 1120–1040 cm^{-1} (ν(Si—O)), 920 cm^{-1} (ν(Al—O—H)), and 796 cm^{-1} (ν(Al(Mg)—O—H)) (Vantelon, Pelletier, Michot, Barres, & Thomas, 2001). Weaker peaks at 3624 cm^{-1} and 1633 cm^{-1} are probably associated with Si—OH stretching and bound water (HOH scissoring). MMT has relatively low absorbance in the 1400–1300 cm^{-1} range, which will be useful below.

The FTIR spectrum for 10 wt% MMT–levan appears to be very similar to that of pure levan. The absorbance peak magnitudes differ for at least three reasons: the films had different thicknesses; the composite film contained 10 wt% MMT; and specific

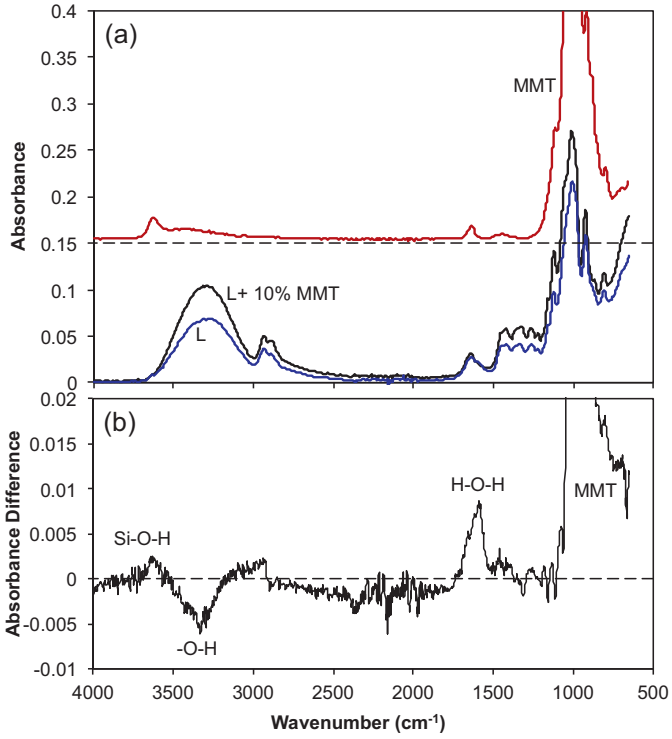

Fig. 2. (a) FTIR absorbance spectra for pure levan (L), 10 wt% MMT–levan composite, and pure MMT (shifted upwards by 0.15 absorbance units for clarity). (b) Absorbance difference between the rescaled levan spectrum (as described in the text) and that for 10 wt% MMT–levan composite.

MMT–levan interactions could enhance or suppress certain peaks. Because we (unfortunately) do not have a record of the film thicknesses for these samples, we re-scaled the levan spectrum (Fig. S9) in order to minimize the absorbance difference between the 10 wt% MMT–levan and pure levan spectra over the 1400–1300 cm^{-1} range, where MMT has minimal absorbance. Fig. 2b shows the absorbance difference (ΔA), calculated as "MMT–levan minus rescaled, pure levan". If the two films differed only in thickness, ΔA would equal zero at all wavenumbers.

In fact, ΔA shows a strong positive value for wavenumbers below 1100 cm^{-1} due to the presence of MMT in the composite film. Another positive ΔA peak, centered at 1636 cm^{-1}, indicates that the composite has a higher concentration of bound water than the pure levan film. We see small positive ΔA peaks at 3650 cm^{-1} and 2973 cm^{-1}, perhaps also due to the presence of MMT in the composite film. The most significant *negative* ΔA peak, centered at 3330 cm^{-1}, suggests that MMT–levan interactions result in suppression of OH stretching. If MMT–levan composite only had additional bound water, we might expect to see a positive ΔA peak in the OH stretching region. Taken together, the evidence suggests that levan has an attractive interaction with MMT via hydrogen bonding, mediated by bound water, between levan hydroxyls and MMT's surface oxygen and edge hydroxyl groups.

3.3. Optical properties

Extruded levan sheets containing high levels of glycerol plasticizer (Barone & Medynets, 2007) are optically opaque. In general, solution-cast films of pure levan appear to be optically clear; the clarity of MMT–levan composites decreases with increasing MMT loading. These observations are quantified by optical absorbance data shown in Fig. 3. MMT–levan composites with less than 20 wt% MMT have good clarity (>80% transmittance) for light at optical wavelengths (400–800 nm).

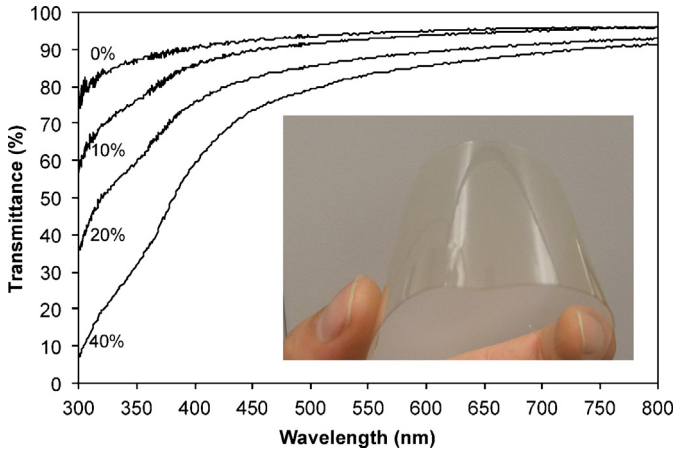

Fig. 3. Optical transmittance as a function of wavelength for pure levan (0%) and MMT–levan composites (curves labeled with wt% MMT). Inset: photograph of a 5 wt% MMT–levan composite film illustrating its transparency and flexibility.

3.4. Thermal properties

3.4.1. TGA analysis

TGA provides information on the water content of samples and the effect of MMT on levan thermal stability. Upon heating in air, levan and MMT–levan composites undergo several stages of thermal degradation (Fig. 4). These samples were previously dried (80 °C, 24 h, vacuum) to remove water. Up to 200 °C, pure levan loses about 6% of its weight, perhaps due to residual moisture and early decomposition; the weight losses of MMT–levan composites are all less than 3%. All of the samples manifest significant weight loss (30–35%) between 200 and 250 °C. The rate of weight loss is also greatest over this temperature range. The TGA data show (Fig. 4a) that addition of 1 wt% MMT to levan increases the onset temperature for thermal degradation by 6–8 °C, depending on how one defines the onset. For example, we measured 10% weight loss at 221.8 °C for 1 wt% MMT–levan, a value 8.1 °C greater than that for pure levan (213.7 °C).

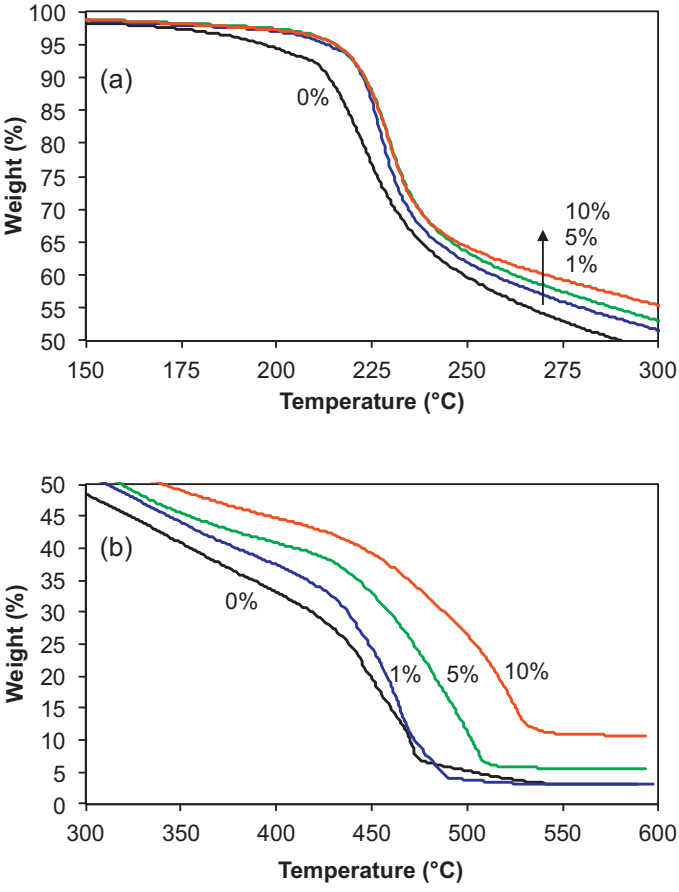

Fig. 4. TGA sample weight as a function of temperature for pure levan (0%) and MMT–levan composites (curves labeled with wt% MMT). Samples were dried in a vacuum oven (80 °C, 24 h) prior to TGA measurement. Panels (a) and (b) focus on lower and higher temperature ranges.

From 250 to 425 °C, the samples continue to lose weight (additional 25–32%), but at a lower rate than at lower temperatures. Between 425 and 450 °C, the samples enter a final stage of decomposition; the onset and ending temperatures of this stage increase, and the decomposition rate decreases, with increasing MMT loading (Fig. 4b). The final sample weights correlate with the initial MMT loading.

The features of levan thermal decomposition observed here are similar to those observed previously for unhydrolyzed *Streptococcus salivarius* levan (Stivala, Kimura, & Reich, 1981). That work speculated that as temperature increases, levan's $\beta(2\rightarrow1)$ branch point linkages break first, followed by main chain $\beta(2\rightarrow6)$ linkages, pyranose rings, and other char-forming reactions. Correlating these decomposition mechanisms with observed TGA weight loss stages is beyond the scope of this study. The presence of MMT clay may reduce the rates of levan decomposition reactions. More likely, the MMT creates a barrier that hinders the ingress of oxygen and the escape of decomposition products. The barrier effect certainly plays a role in retarding the final stage of decomposition, where we observe a direct correlation between initial MMT loading and the onset and ending temperatures of the final stage of decomposition.

"Pre-dried" samples (discussed above) lose 3–6% of their initial weight upon heating from ambient temperature to 200 °C in air. For samples stored under ambient lab conditions (23 ± 1 °C and 55 ± 2% RH), TGA weight loss measurements (Fig. S10) indicate that levan and MMT–levan composite samples lose 12–15% of their initial weight over the same temperature range. The majority of this weight loss is due to water absorbed by the samples from ambient humid air. This absorbed water is crucial because it plasticizes the levan, enabling the preparation of intact films.

3.4.2. DSC analysis

Dried samples of levan and MMT–levan films were subjected to the DSC heat-cool-heat thermal cycle described earlier. The first heating scans (not shown) manifested slope changes between 130 °C and 150 °C that were not reproduced in the subsequent cooling and heating scans. This feature could be due to evaporation of residual bound water that was not removed in the sample drying protocol. The first cooling scans (not shown) and second heating scans (Fig. 5) show reproducing step transitions that we identify as glass transitions. Pure levan has a glass transition temperature (T_g) at 75.5 °C, a value significantly less than the value (141 °C) previously reported for *Baccilus* sp. levan from the same source (Manadhar et al., 2009). We cannot explain this difference, but speculate that the previous measurement may have been influenced by residual water in the samples.

The T_g values shift to higher temperatures with increasing MMT loading (Fig. 5). For example, adding 1 wt% MMT to levan increases T_g by nearly 33–108.3 °C. The T_g of 10 wt% MMT–levan is 50 °C higher than pure levan. The breadth of the glass transition zone broadens from about 19 °C for pure levan to 23–25 °C for the composites. These results provide evidence of intimate mixing and a strong, attractive levan–MMT interaction. Below T_g in the composites, the strength of the interaction retards the levan's long-range molecular motions relative to those of pure levan at the same temperature.

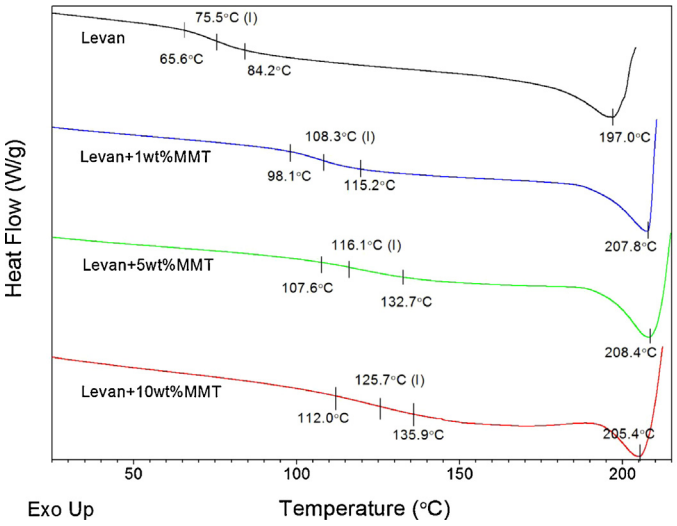

Fig. 5. DSC heat flow as a function of temperature for pure levan and MMT–levan composites.

The second heating scans show an apparent melting transition at 197 °C for pure levan and above 205 °C in MMT–levan composites. However, TGA results indicated the onset of thermal decomposition at temperatures around 200 °C. Thus the designation of this transition as melting cannot be definitive. If levan and MMT–levan composites do have a melting transition, it certainly overlaps with the onset of thermal decomposition. Nonetheless, the DSC results concur with those from TGA, showing that the MMT significantly improves the thermal stability of levan.

3.5. Composite mechanical properties

Films of levan and MMT–levan composites, equilibrated with air at 50–60% RH, are flexible (Fig. 3) because they are plasticized by approximately 10 wt% water (Fig. S11). However, the film samples lose their flexibility and become brittle when dried, and they lose strength at higher humidity levels. These qualitative observations indicate that water plasticization plays an important role governing the mechanical properties of levan and MMT–levan composites. This work quantifies only the mechanical properties of levan and MMT–levan films equilibrated with ambient laboratory air, consistently maintained at 23 ± 1 °C and 60 ± 1% RH.

Fig. 6 shows the mechanical properties of levan and MMT–levan composites subjected to small-amplitude oscillatory tensile loads via DMA. Table S1 (Supporting information) provides values of these quantities at selected frequencies. With increasing frequency, the storage and loss moduli (G' and G'') both increase, and loss tangent ($\tan\delta$) decreases. No glass transition is apparent in this data. Smaller G' values at low frequency characterize slower, the more viscous, longer-range deformation of levan's molecular network; larger G' values at high frequency characterize more elastic, shorter-range intra- and intermolecular interactions. The $\tan\delta$ values are less than unity, implying that levan and MMT–levan composites are viscoelastic solids. At all frequencies, the values of G', G'', and tanδ for pure levan and 1 wt% MMT–levan do not differ significantly. Thus adding 1 wt% MMT does not improve levan's mechanical properties, at least for small-amplitude tensile loading.

However, for 5 and 10 wt% loading levels, adding MMT to levan significantly increases G'. To illustrate this more clearly, Table 1 shows the "relative" storage modulus, $G'_r \equiv G'_{MMT}(wt\%)/G'_{levan}$, at four selected frequencies as a function of MMT loading. Adding 10 wt% MMT to levan leads to G'_r values as high as 5.3, equivalent to a 430% increase in G' relative to that of levan. G'_r increases

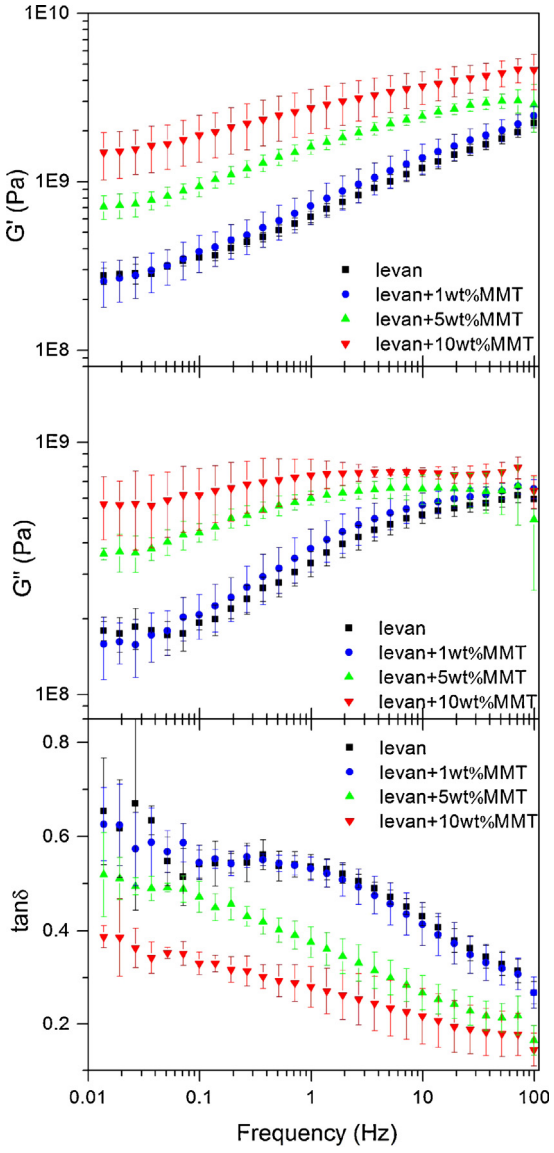

Fig. 6. Storage modulus (G'), loss modulus (G''), and loss tangent ($\tan\delta$) as functions of deformation frequency for pure levan and MMT–levan composites subjected to small amplitude oscillatory tensile testing via DMA. Measurements performed in air under ambient conditions (23 °C and 60% RH). The values are averages over five specimens, and the error bars are standard deviations.

with MMT loading for all deformation frequencies, but the impact is greatest for low frequencies (0.1 and 1.0 Hz). This observation suggests that the strong MMT–levan interaction restricts or inhibits the slower, larger-scale motions of the levan molecular network. Faster, shorter-range molecular deformations probed at high frequencies (e.g., 100 Hz) are less influenced by the presence of MMT until the loading reaches 10 wt%. The upturn in G'_r seems to occur

Table 1
Relative storage modulus (G'_r) as a function of MMT loading (wt%) at the indicated deformation frequencies from small amplitude oscillatory tensile testing via DMA. Measurements performed in air under ambient conditions (23 °C and 60% RH).

Sample	Frequency (Hz)			
	0.1	1.0	10	100
Levan	1.00 ± 0.12	1.00 ± 0.07	1.00 ± 0.09	1.00 ± 0.06
1 wt% MMT–levan	1.08 ± 0.27	1.16 ± 0.26	1.15 ± 0.23	1.08 ± 0.14
5 wt% MMT–levan	2.63 ± 0.34	2.59 ± 0.25	2.03 ± 0.16	1.26 ± 0.40
10 wt% MMT–levan	5.33 ± 1.66	4.41 ± 1.29	3.07 ± 0.69	2.02 ± 0.48

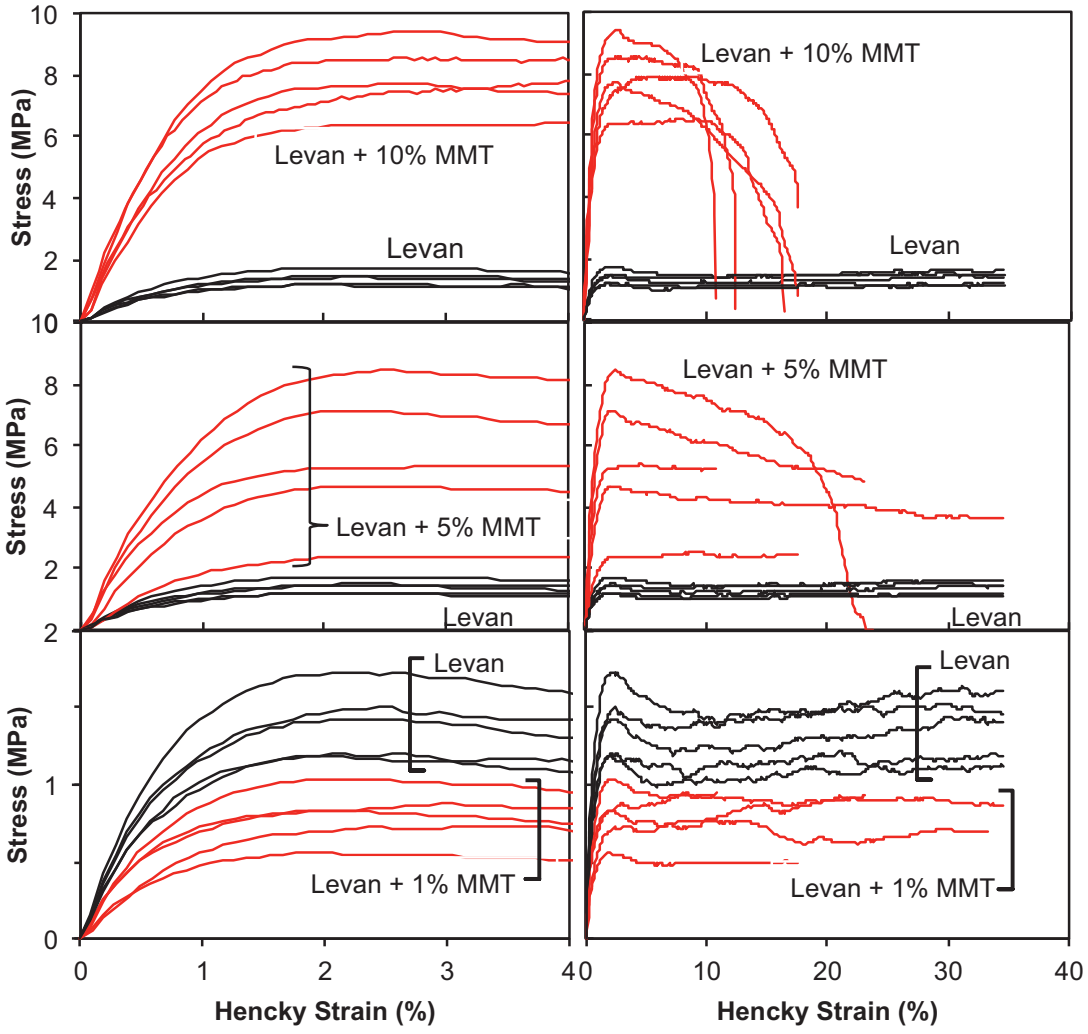

Fig. 7. Tensile stress as a function of applied strain for pure levan and MMT–levan composites (as labeled in the plots). Left column shows 0–4% strain; right column shows 0–40% strain. Measurements performed in air under ambient conditions (23 °C and 60% RH).

between 1 and 5 wt% MMT, which coincides with the concentration range expected for the isotropic–nematic transition in the MMT nanostructure.

Tensile stress–strain curves for levan and MMT–levan composites (Fig. 7) show typical ductile behavior. Pure levan and 1 wt% MMT–levan have qualitatively similar stress–strain curves with yield points at about 2% strain and deformations-at-break of 20–35%. However, 1 wt% MMT–levan has significantly lower Young's modulus and yield stress than pure levan (Table 2). Adding 1 wt% MMT thus has a detrimental effect on levan's mechanical properties under finite tensile deformations. MMT could provide mechanical reinforcement by creating "physical crosslinks" via its strong interaction with levan (implied by DSC results). However, if MMT platelets are too far apart to be bridged by levan molecules, then the MMT may not contribute to the load-carrying physical network in the composite. Moreover, the presence of MMT platelets certainly disrupts levan's molecular entanglement and network structure, possibly explaining the negative impact of MMT on mechanical properties.

Table 2
Tensile properties of levan and levan–MMT composites.

Sample	Young's modulus (GPa)	Yield stress (MPa)	Yield strain (%)
Levan	0.167 ± 0.023	1.407 ± 0.225	2.208 ± 0.083
1 wt% MMT–levan	0.095 ± 0.023	0.797 ± 0.177	2.134 ± 0.151
5 wt% MMT–levan	0.556 ± 0.214	5.573 ± 2.340	2.212 ± 0.126
10 wt% MMT–levan	0.874 ± 0.147	7.805 ± 1.112	2.244 ± 0.044

In contrast, the tensile behavior of 10 wt% MMT–levan composite differs qualitatively (Fig. 7) and quantitatively (Table 2) from that of pure levan. The Young's modulus of this composite is 424% greater than that of pure levan, the yield stress is 454% greater, and the toughness (area under curve up to 10% strain) is 485% greater. Adding 10 wt% MMT clearly has a remarkable, positive effect on levan's mechanical properties under finite tensile deformations. In this case, MMT platelets are certainly close enough to be bridged by levan molecules. Furthermore, due to the loading level and high aspect ratio, the MMT platelets likely have considerable nematic order, as suggested by XRD results (Fig. 1) and our earlier calculations. This suggests a physical picture in which the MMT platelets, aligned and "glued" together by levan molecules, create a distinct filler network structure within the levan matrix (Fig. 8). This MMT network structure can carry a significant load and work in parallel with levan's molecular network to provide significant mechanical reinforcement.

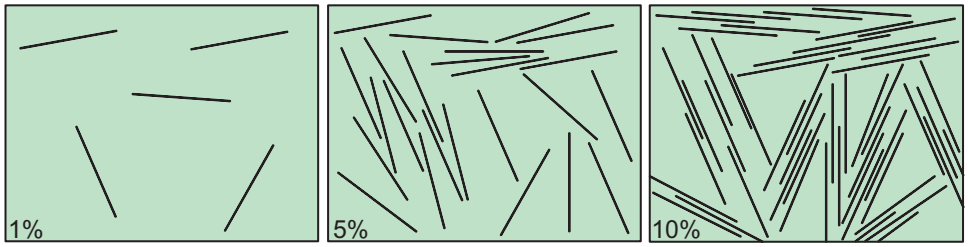

Fig. 8. Schematic illustration of MMT platelets dispersed in levan. The lines, representing MMT platelets, have an aspect ratio of 100 (length to width). The lines occupy 0.5%, 2.5%, and 5.2% of the area of each panel (left to right), qualitatively corresponding to 1, 5, and 10 wt% MMT in levan. In three-dimensional mixtures of non-interacting, exfoliated MMT platelets, we expect the isotropic–nematic transition to begin at 1.6 vol% (3.1 wt%) MMT.

The tensile behavior of the 5 wt% MMT–levan composite lies somewhere in between pure levan and the 10 wt% composite (Fig. 7). Some of the stress–strain curves for 5 wt% MMT–levan resemble those of pure levan, and others look like those of the 10 wt% composite. The average values of Young's modulus and yield stress for 5 wt% MMT–levan (Table 2) are significantly higher than those of pure levan and 1 wt% MMT–levan, but the standard deviation values are relatively large. This variability suggests that the 5 wt% MMT loading may be near the threshold for the formation of a levan-bridged MMT network. Our earlier calculation gave an estimate of 3 wt% for the onset of the isotropic–nematic transition. At 5 wt% loading, the MMT–levan composite could have coexisting regions of isotropic and nematic order, perhaps rationalizing the scatter observed in the stress–strain curves, Young's modulus, and yield stress values.

4. Conclusions

This work shows, for the first time, that solution blending and film coating can be used to prepare transparent, flexible, tough MMT–levan composite films. Comparing FTIR spectra of levan and MMT–levan composite provides evidence that levan interacts with MMT via water-mediated hydrogen bonding involving levan's hydroxyl groups. MMT loading as low as 1 wt% significantly improves levan's thermal stability and increases T_g by up to 33 °C. This implies that the levan–MMT interaction is attractive and strong enough to change levan's thermal properties. Adding 1 wt% MMT to levan leaves its tensile properties unchanged for small amplitude oscillatory loading. However, 1 wt% MMT has a negative impact on levan's tensile properties under finite strain loading. We speculate that MMT platelets disrupt levan's molecular entanglement, but the platelets are too far apart to be bridged by adsorbed levan molecules (Fig. 8, left panel).

Higher MMT loadings (5 and 10 wt%) result in significant mechanical reinforcement of levan. The storage modulus (small amplitude oscillatory loading) and Young's modulus (finite strain tensile loading) both increase in proportion to MMT loading, as high as 480% relative to pure levan. The 10 wt% MMT–levan composite has optical transmittance almost as high as pure levan, which implies that the composite does not contain a high level of MMT aggregates that would scatter light at optical wavelengths. XRD patterns for these composites show a broad diffraction peak at 9.4° (2θ) that corresponds to the (0 0 1) reflection from MMT platelets with d = 1.88 nm. This value, 0.62 nm greater than that of the initial MMT powder, probably represents re-stacked MMT platelets coated by adsorbed, uncoiled levan molecules. The 9.4° peak is barely visible in the 5 wt% MMT–levan composite, possibly because only at this loading level does the peak intensity exceed that of the background.

However, the appearance and intensity growth of the 9.4° peak in the XRD patterns of 5 and 10 wt% MMT composites can also be rationalized in terms of an isotropic–nematic transition in MMT platelet orientation (Fig. 8, center and right panels). For non-interacting disks with the same average aspect ratio as our MMT platelets (Fig. S9), theory predicts a transition from single phase isotropic to a two-phase mixture of isotropic and nematic (aligned) orientations at a platelet loading of 1.6 vol%, corresponding to 3.1 wt% for MMT–levan mixtures. Of course, our MMT platelets are polydisperse and interact via adsorbed levan (bridging attraction, steric repulsion, or something in between). A strong, levan-mediated bridging interaction would certainly favor restacking of platelets and nematic order.

The combination of levan-mediated platelet bridging and nematic ordering may produce a platelet network structure responsible for the remarkable level of mechanical reinforcement of the levan matrix. More work is needed to understand the role of water in MMT–levan interactions and to maintain ductility when the composites are dried. Nonetheless, this work shows, for the first time, that the thermal and mechanical properties of a microbial polysaccharide, levan, can be greatly enhanced by solution blending with a few weight percent of exfoliated MMT platelets.

Acknowledgments

We thank Dr. Joan Combie (Montana Polysaccharides) for providing the *Bacillus sp.* levan used in this work. We thank Chunyan Liu, Jennifer Guerrero-Medina, Arief Wibowo, and the late Julius Brown for their assistance in collecting some of the data presented in this work. The U.S. National Science Foundation (award IIP-0650186) and the University of South Carolina provided funding for this work.

Appendix A. Supplementary data

Supplementary data associated with this article can be found, in the online version, at http://dx.doi.org/10.1016/j.carbpol.2013.09.073.

References

Arvidson, S. A., Rinehart, B. T., & Gadala-Maria, F. (2006). Concentration regimes of solutions of levan polysaccharide from *Bacillus* sp. *Carbohydrate Polymers*, *65*, 144–149.

Bahary, W. S., Stivala, S. S., Newbrun, E., & Ehrlich, J. (1975). Levans. III. A light-scattering study of streptococcus salivarious levan in dimethyl sulfoxide. *Biopolymers*, *14*, 2467–2478.

Barone, J. R., & Medynets, M. (2007). Thermally processed levan polymers. *Carbohydrate Polymers*, *69*, 554–561.

Bates, M. A. (1999). Influence of particle shape on the nematic–isotropic transition of colloidal platelet systems. *Journal of Chemical Physics*, *111*, 1732–1736.

Bates, M. A., & Frenkel, D. (1999). Nematic–isotropic transition in polydisperse systems of infinitely thin hard platelets. *Journal of Chemical Physics*, *110*, 6553–6559.

Bodie, E. A., Schwartz, R. D., & Catena, A. (1985). Production and characterization of a polymer from arthrobacter sp. *Applied and Environmental Microbiology*, *50*(3), 629–633.

Chivrac, F., Pollet, E., & Averous, L. (2009). Progress in nano-biocomposites based on polysaccharides and nanoclays. *Materials Science and Engineering Reports*, *67*, 1–17.

Combie, J. (2006). Polysaccharids for drug delivery and pharmaceutical applications. In R. H. Marchessault, F. Ravenelle, & X. X. Zhu (Eds.), *ACS symposium series, Vol. 934*. Washington, DC: ACS Publications.

French, A. D. (1989). Chemical and physical properties of fructans. *Journal of Plant Physiology*, *134*, 125–136.

Grube, M., Bekers, M., Upite, D., & Kaminska, E. (2002). Infrared spectra of some fructans. *Spectroscopy*, *16*, 289–296.

Han, Y. W., & Watson, M. A. (1992). Production of microbial levan from sucrose, sugarcane juice and beet molasses. *Journal of Industrial Microbiology*, *9*, 257–260.

Harnau, L. (2008). Structure and thermodynamics of platelet dispersions. *Molecular Physics*, *106*, 1975–2000.

Huber, A. E., Stayton, P. S., Viney, C., & Kaplan, D. L. (1994). Liquid crystallinity of a biological polysaccharide: The levan/water phase diagram. *Macromolecules*, *27*, 953–957.

Huber, A. E., & Viney, C. (1997). Chimetic liquid crystallinity: Nonconvalent association of DNA and bacterial levan. *Macromolecules*, *30*, 2662–2670.

Huber, A. E., & Viney, C. (1998). Supramolecular liquid crystallinity: Spherical coils of levan surrounding cylindrical rods of DNA. *Physical Review Letters*, *80*, 623–626.

Ingelman, B., & Siegbahn, K. (1944). Dextran and levan molecules studied with the electron microscope. *Nature*, *154*, 237–238.

Johansson, C., Bras, J., Mondragon, I., Nechita, P., Plackett, D., Simon, P., et al. (2012). Renewable fibers and bio-based materials for packaging applications – A review of recent developments. *BioResources*, *7*(2), 2506–2552.

Kasapis, S., Morris, E. R., Gross, M., & Rudolph, K. (1994). Solution properties of levan polysaccharide from *Pseudomonas syringae* p. *phaseolicola*, and its possible primary role as a blocker of recognition during pathogenesis. *Carbohydrate Polymers*, *23*, 55–64.

Kang, S. A., Jang, K.-H., Seo, J.-W., Kim, K. H., Kim, Y. H., Rairakhwada, D., et al. (2009). Levan: Applications and perspectives. In B. H. A. Rehm (Ed.), *Microbial production of biopolymers and polymer precursors: Applications and perspectives* (pp. 145–160). Norfolk, UK: Caister Academic Press.

Keith, J., Wiley, B., Ball, D., Arcidiacono, S., Zorfass, D., Mayer, J., et al. (1991). Continuous culture system for production of biopolymer levan using Erwinia herbicola. *Biotechnology and Bioengineering*, *38*(5), 557–560.

Khorramian, B. A., & Stivala, S. S. (1982). Assessment of branching in hydrolysates of *S. salivarius* levan and *L. mesenteroides* dextran from small-angle X-ray scattering. *Carbohydrate Research*, *108*, 1–11.

Kim, K. H., Chung, C. B., Kim, Y. H., Kim, K. S., Han, C. S., & Kim, C. H. (2005). Cosmeceutical properties of levan produced by *Zymomonas mobilis*. *Journal of Cosmetic Science*, *56*, 395–406.

Kochumalayil, J. J., Bergenstrahle-Wohlert, M., Utsel, S., Wagberg, L., Zhou, Q., & Berglund, L. A. (2013). Bioinspired and highly oriented clay nanocomposites with xyloglucan biopolymer matrix – Extending the range of mechanical and barrier properties. *Biomacromolecule*, *14*(1), 84–91.

Küçülaşik, F., Kazak, H., Guney, D., Finore, I., Poli, A., Yenigun, O., et al. (2011). Molasses as fermentation substrate for levan production by *Halomonas* sp. *Applied Microbiology Biotechnology*, *89*, 1729–1740.

Liu, J., Luo, J., Ye, H., Sun, Y., Lu, Z., & Zeng, X. (2010). Medium optimization and structural characterization of expopolysaccharides from endophytic bacterium *Paenibacillus polymyxa* EJS-3. *Carbohydrate Polymers*, *79*, 206–213.

Majeed, K., Jawaid, M., Hassan, A., Bakar, A. A., Khalil, H. P. S. A., Salema, A. A., et al. (2013). Potential materials for food packaging from nanoclay/natural fibres filled hybrid composites. *Materials and Design*, *46*, 391–410.

Manadhar, S., Vidhate, S., & D'Souza, N. (2009). Water soluble levan polysaccharide biopolymer electrospun fibers. *Carbohydrate Polymers*, *78*, 794–798.

Newbrun, E., Lacy, R., & Christie, T. M. (1971). Morphology and size of extracellular polysaccharides from oral streptococci. *Archives of Oral Biology*, *16*(8), 863–872.

Onsager, L. (1949). The effects of shape on the interaction of colloidal particles. *Annals of the New York Academy of Sciences*, *51*, 627–659.

Ploehn, H. J., & Liu, C. Y. (2006). Quantitative analysis of montmorillonite platelet size by atomic microscopy. *Industrial and Engineering Chemistry Research*, *45*, 7025–7034.

Poli, A., Kazak, H., Gurleyendag, B., Tommonaro, G., Pieretti, G., Oner, E. T., et al. (2009). High level synthesis of levan by a novel *Halomonas* species growing on defined media. *Carbohydrate Polymers*, *78*, 651–657.

Rhim, J.-W., & Ng, P. K. W. (2007). Natural biopolymer-based nanocomposite films for packaging applications. *Critical Reviews in Food Science and Nutrition*, *47*, 411–433.

Seymour, F. R., Knapp, R. D., & Jeanes, A. (1979). Structural analysis of levans by use of ^{13}C NMR spectroscopy. *Carbohydrate Research*, *72*, 222–228.

Simms, P. J., Boyko, W. J., & Edwards, J. R. (1990). The structural analysis of a levan produced by *Streptococcus salivarius* SS2. *Carbohydrate Research*, *208*, 193–198.

Sinha Ray, S., & Bousmina, M. (2005). Biodegradable polymers and their layered silicate nanocomposites: In greening the 21st century materials world. *Progress in Materials Science*, *50*, 962–1079.

Sorrentino, A., Gorrasi, G., & Vittoria, V. (2007). Potential perspectives of bio-nanocomposites for food packaging applications. *Trends in Food Science & Technology*, *18*, 84–95.

Stivala, S. S., Bahary, W. S., Long, L. W., Ehrlich, J., & Newbrun, E. (1975). Levans. II. Light-scattering and sedimentation data of streptococcus salivarius levan in water. *Biopolymers*, *14*, 1283–1292.

Stivala, S. S., & Khorramian, B. A. (1982). Assessment of branching in *S. salivarius* levan from small-angle X-ray scattering. *Carbohydrate Research*, *101*, 1–11.

Stivala, S. S., Kimura, J., & Reich, L. (1981). Thermal degradation of levan. *Thermochimica Acta*, *50*, 111–122.

Tang, X. Z., Kumar, P., Alavi, S., & Sandeep, K. P. (2012). Recent advances in biopolymers and biopolymer-based nanocomposites for food packaging materials. *Critical Reviews in Food Science and Nutrition*, *52*, 426–442.

Unlu, C. H., Gunister, E., & Atici, O. (2009). Synthesis and characterization of NaMt biocomposites with cor cob xlan in aqueous media. *Carbohydrate Polymers*, *76*, 585–592.

van der Beek, D., Reich, H., van der Schoot, P., Dijkstra, M., Schilling, T., Vink, R., et al. (2006). Isotropic–nematic interface and wetting in suspensions of colloidal platelets. *Physical Review Letters*, *97*(8), 087801.

van der Kooij, F. M., Kassapidou, K., & Lekkerkerker, H. N. W. (2000). Liquid crystal phase transitions in suspensions of polydisperse plate-like particles. *Nature*, *406*, 868–871.

van der Kooij, F. M., & Lekkerkerker, H. N. W. (1998). Formation of nematic liquid crystals in suspensions of hard colloidal platelets. *Journal of Physical Chemistry B*, *102*, 7829–7832.

van Dyk, J. S., Kee, N. L. A., Frost, C. L., & Pletschke, B. I. (2012). Extracellular polysaccharide production in bacillus licheniformis svd1 and its immunomodulatory effect. *BioResources*, *7*(4), 4976–4993.

Vantelon, D., Pelletier, M., Michot, L. J., Barres, O., & Thomas, F. (2001). Fe, Mg and Al distribution in the octahedral sheet of montmorillonites. An infrared study in the OH-bending region. *Clay Minerals*, *36*, 369–379.

Velazquez, G., Herrera-Gomez, A., & Martin-Polo, M. O. (2003). Identification of bound water through infrared spectroscopy in methylcellulose. *Journal of Food Engineering*, *59*, 79–84.

Viota, J. L., Lopez-Viota, M., Saake, B., Stana-Kleinschek, K., & Delgado, A. V. (2010). Organoclay particles as reinforcing agents in polysaccharide films. *Journal of Colloid and Interface Science*, *347*, 74–78.

Vroege, G. J., & Lekkerkerker, H. N. W. (1992). Phase transitions in lyotropic colloidal and polymer liquid crystals. *Reports on Progress in Physics*, *55*, 1241–1309.

Yu, L., Dean, K., & Li, L. (2006). Polymer blends and composites from renewable resources. *Progress in Polymer Science*, *2006*, 576–602.